UNIVERSITY OF BIRMINGHAM
University of Birmingham Research at Birmingham

On the application of the anisotropic enhanced thermal conductivity approach to thermal modelling of laser-based powder bed fusion processes

Nikam, S.; Wu, H.; Harkin, R.; Quinn, J.; Lupoi, R.; Yin, S.; McFadden, S.

DOI:
10.1016/j.addma.2022.102870

License:
Creative Commons: Attribution-NonCommercial-NoDerivs (CC BY-NC-ND)

Document Version
Peer reviewed version

Citation for published version (Harvard):
Nikam, S, Wu, H, Harkin, R, Quinn, J, Lupoi, R, Yin, S & McFadden, S 2022, 'On the application of the anisotropic enhanced thermal conductivity approach to thermal modelling of laser-based powder bed fusion processes', *Additive Manufacturing*, vol. 55, 102870. https://doi.org/10.1016/j.addma.2022.102870

Link to publication on Research at Birmingham portal

General rights
Unless a licence is specified above, all rights (including copyright and moral rights) in this document are retained by the authors and/or the copyright holders. The express permission of the copyright holder must be obtained for any use of this material other than for purposes permitted by law.

•Users may freely distribute the URL that is used to identify this publication.
•Users may download and/or print one copy of the publication from the University of Birmingham research portal for the purpose of private study or non-commercial research.
•User may use extracts from the document in line with the concept of 'fair dealing' under the Copyright, Designs and Patents Act 1988 (?)
•Users may not further distribute the material nor use it for the purposes of commercial gain.

Where a licence is displayed above, please note the terms and conditions of the licence govern your use of this document.

When citing, please reference the published version.

Take down policy
While the University of Birmingham exercises care and attention in making items available there are rare occasions when an item has been uploaded in error or has been deemed to be commercially or otherwise sensitive.

If you believe that this is the case for this document, please contact UBIRA@lists.bham.ac.uk providing details and we will remove access to the work immediately and investigate.

Download date: 19. Apr. 2024

On the application of directional correction factors for a computationally efficient thermal model of laser-based powder bed fusion processes

Sagar Nikam[a], Hao Wu[a], Ryan Harkin[a], Justin Quinn[a], Rocco Lupoi[b], Shou Yin[b], Shaun McFadden[a,*]

[a] School of Computing, Engineering, and Intelligent Systems, Ulster University, Magee Campus, Northland Road, Derry/Londonderry, Northern Ireland, UK BT48 7JL

[b] Department of Mechanical, Manufacturing and Biomedical Engineering, Trinity College Dublin, Parsons Building, Dublin, Ireland, D2

[*] corresponding author: s.mcfadden2@ulster.ac.uk

Keywords: Additive Manufacturing; Powder bed fusion; Heat conduction model; Marangoni convection; Directional correction factor; Melt pool dimensions

Abstract

Computational simulation of the Powder Bed Fusion (PBF) process is a useful tool for predicting and analysing melt pool geometry during the deposition process. Advanced modeils that use Computational Fluid Dynamics (CFD) can accurately simulate the complex melt pool dynamics of the process but are typically computationally expensive and time consuming to implement. CFD models require thermophysical data over a large temperature range that may be difficult to acquire for the material systems of interest. Heat conduction models, which are useful to industrial end users are easier and faster to implement, but their accuracy can be compromised. The main difference between heat conduction and CFD modelling is the absence of convection (especially Marangoni convection) in the heat conduction model. However, several sources in literature have highlighted a simple approach to mimicking the effects of Marangoni convection on the melt pool by artificially and uniformly increasing the thermal conductivity of liquid by a constant correction factor. However, due to its simplicity and the lack of agreement within literature, the modified heat conduction approach is neither sufficiently robust nor universally consistent. In the present work, the heat conduction model is modified using an orthotropic description of anisotropic thermal conductivity in the liquid phase by applying directional correction factors. The correction factors are calibrated by comparing the predicted geometry against experimentally-obtained melt pool dimensions for single-layer, multiple tracks in Ti-6Al-4V processed by laser-PBF. After appropriate correction factors were selected, the modified heat conduction model gave results in good agreement with experiments. To test the general applicability of the approach, data from literature were analysed and simulated using the model. After correction factors were adjusted accordingly, the simulated results were validated over the range of power levels and scan speeds.

1. Introduction

Computational simulation of melt pool dynamics for the Powder Bed Fusion (PBF) process is important but also computationally complex and time consuming to implement. A Computational Fluid Dynamics (CFD) model with descriptions of the correct physical phenomenon included has to be capable of predicting the outcomes of localised melting, melt pool fluid dynamics, and solidification in the PBF process. Important outcomes from simulations include predictions of the thermal response; the size and shape of the melt pool (length, width, and depth); and the geometry of the consolidated material deposited on the substrate (either on the starting platform or on the previous layer). The temperature gradients and cooling rates within the melt pool influence solidification kinetics, microstructure development, and defect initiation in the process. Additionally, previously-deposited solid will experience repeated heat cycles due to layer addition that can cause solid-state transformations or residual stresses within the additively manufactured part.

Melt pool width and depth are used as predictors of lack-of-fusion defects [1] which, in turn, can be used to determine the deposition rate [2]. A simple geometrical relationships for melt pool width-to-hatch spacing and depth-to-layer height can, with the application of a predictive thermal model, be translated onto a laser power (P) versus scan speed (v) diagram thus giving a bounding line for the optimal process parameter window in P-v space [3]. Gordon et al. [3] used the classic Rosenthal model [4] combined with the geometrical criterion of Tang et al. [1] to calculate the processing boundary for lack-of-fusion. Rosenthal's equation is based on steady-state heat conduction, zero latent heat and constant thermophysical properties – it is the simplest model to describe a moving point heat source in a substrate. Indeed, Rosenthal's model assumes that all heat input is through a single point at the origin of heat application and gives the unrealistic result of infinite temperature at that point of application. Nevertheless, as it is simple to use, the Rosenthal equation is used widely to predict the 2D thermal field and melt pool width for welding and additive manufacturing. With the assumption of axis-symmetric geometry, the predicted melt pool depth is taken as half of the predicted width. Gordon et al. [3] used Rosenthal's equation in their work and admitted that the purpose of their approach was to generate a practical relationship for lack-of fusion prediction. However, they do suggest that improvements can be obtained with computer modelling of the melt pool geometry; thus, highlighting the importance of advanced modelling to the field of additive manufacturing.

Naturally, several advancements beyond the Rosenthal model have been made. Goldak et al. [5] proposed a finite element model of moving point heat sources that used a Gaussian distribution with the facility to include a double ellipsoidal geometry to cover different welding processes. More recently, models of laser-material interaction are available using CFD approaches. Shu et al. [6] presented a critical review of the modelling approach and highlighted at the importance of convection, in particular Marangoni convection. However, this model, as with every model in this discussion up to this point, did not attempt to model the keyhole effect due to laser beam trapping. The physics of keyholing (as described elsewhere [7]) can lead to keyhole porosity and is beyond the scope of work. Recent work by Jakumeit et al. [8] modelled the complex gas flows that evaporate from the melt pool. Higher line energies were shown to lead to greater evaporation and a transition to keyholing.

To overcome the problems associated with CFD modelling, heat conduction models for moving point heat source have been developed and applied to PBF. In these models, the complexities of melt pool fluid mechanics are ignored thus making it computationally simpler and less time consuming to simulate. These models are sometimes called reduced-physics models because their aim is to provide reasonable results with a consummate level of physics and, hence, computational effort. However, the development (or justification) of a reduced-physics simulation model for PBF processes that balances computational efficiency with reliable results is a challenge. As state-of-the-art synchrotron radiography experiments demonstrate, laser-material interactions in PBF are complex [9]. Advanced physics models, such as [8], use experimental data to validate and develop science-informed assumptions at the length scales of interest (usually at the microscale). Reduced physics models attempt to use informed decisions and relaxed assumptions to get reasonable results at the macroscale of the process. State-of-the-art experimentation and advanced modelling will progress scientific understanding. Reduced physics models are aimed at providing practical solutions at large length scales. Rather than ignoring the physics, reduced physics models ought to be informed by findings from experiments or code-to-code comparisons with validated models.

Several authors have proposed CFD and heat conduction models for thermal, structural, and melt pool dimensions analysis [10,11]. Some report on the development of CFD models for the PBF process using commercial software [12,13] while others report on the development of bespoke codes for PBF processes using heat conduction models [14,15]. What follows is a literature review of the complexities around state-of-the-art melt pool modelling and the

rationale for using heat conduction modelling, leading onto the aims and objectives of the current work.

1.1. Literature review

The review begins by elaborating on selected sources from literature that describe CFD models [19-23] for predicting melt pool dynamics of PBF processes. Afterwards, the focus is placed on purely thermal (heat conduction) and thermomechanical models developed either by neglecting the melt pool fluid dynamics [24-30] or by considering some adaptation for the effects of fluid phenomenon like Marangoni convection [31-34].

Using a CFD model developed for the PBF additive manufacturing process, Xiao and Zhang [16] proposed a model with Marangoni convection and buoyancy effects for the direct metal laser sintering process. They investigated the influence of laser intensity and scanning velocity on the melt pool and found that the laser intensity greatly influences the melt pool dimensions and increasing the scanning velocity tends to shift the melt pool in the opposite travel direction. Xia et al. [17] investigated the porosity evolution for randomly packed powder during selective laser melting of Inconel 718 alloy using a CFD model. The model took into consideration aspects such as phase transition, thermophysical material properties, and interfacial forces. The predicted distribution of porosity was compared with the experimental results and found to be in good agreement. Heeling et al. [18] proposed a CFD model for selective laser melting of stainless steel 316L and IN738LC with the added complexity of fluid flow phenomenon such as Marangoni convection, recoil pressure, evaporation, buoyancy, and capillary effect. They investigated the effect of process parameters such as laser power and scanning speed on remelted melt pool depth and width and found them to be in good agreement with experimental data. Le et al. [19] developed a CFD model with heat transfer and solidification and melting model in ANSYS Fluent for selective laser melting of IN718 alloy. They captured the heat transfer and melt pool dynamics within the melt pool. It was observed that melt pool width and depth were consistent but some variation was observed in the melt pool length for linear and non-linear solidification relationships. Khairallah et al. [20] proposed a CFD model with complex melt pool dynamics of laser PBF processes such as Marangoni convection and recoil pressure. They investigated the fluid flow within the melt pool and the formation of pores, spatter, and denudation zones during the deposition of 316L stainless steel. The CFD model validated against the experimental results was found to be in good agreement.

Li and Gu [21] proposed a 3D heat conduction model to investigate the thermal behaviour during selective laser melting of commercially pure titanium (CP Ti). They investigated the

effect of various combinations of laser power and scanning speed on the thermal analysis and melt pool dimensions of the deposition process. Foroozmehr et al. [22] proposed a volumetric heat source model with an optical penetration depth and predicted melt pool dimensions during deposition of stainless steel 316L when processed by a selective laser melting process. The model was validated against experimental melt pool dimensions that revealed that the melt pool size reached a stable condition after few tracks. Loh et al. [23] proposed a Finite Element (FE) heat transfer model using COMSOL software with added complexity such as volume shrinkage and evaporation during the deposition. They validated this model with experimental values of melt pool dimensions obtained for depositing Aluminium Alloy (6061) on different base plate materials. Huang et al. [24] reported on a heat conduction model of Ti-6Al-4V. They investigated the effect of process parameters, volume shrinkage, and time step on the temperature distribution and melt pool dimensions. It was found that volume shrinkage significantly influenced the temperature and melt pool dimensions; hence, they proposed that it should be considered in the heat conduction model. Teng et al. [25] proposed a model for single layer deposition of Co-Cr material under a selective laser melting process. The model was validated for a single layer and was further extended to capture lack of fusion porosity. The model was experimentally validated and could predict lack of fusion porosity with good agreement. Apart from thermal analysis, several researchers proposed a thermomechanical model for the PBF process. Hodge et al. [26] developed a thermomechanical model for selective laser melting of 316L stainless steel. The model was used to compute and validate the stress and deformation in components of different shapes. For a similar process, Liu et al. [27] proposed a thermomechanical model with a characteristic time-based, heat-input model. The thermal and residual stress analyses predicted with different heat inputs were captured and the computation time was compared for each model. The model was validated by comparing the predicted and actual melt pool dimensions measured for Ti-6Al-4V depositions.

One of the main criticisms of heat conduction models is that they neglect the effects of Marangoni convection within the melt pool. Generally with metal alloys, surface tension in a liquid reduces as temperature increases. When there is a negative temperature gradient along a melt pool surface, then correspondingly, there is a positive surface tension gradient across the liquid surface. This change in surface tension sets up a fluid flow phenomenon with a driving force parallel to the surface. This is known as the Marangoni effect. The Marangoni effect has been observed using x-ray radiographic technology [28]. This effect plays an important role on the melt pool temperature and geometry. Essentially, due to fluid mixing, the peak temperatures

are therefore smaller than those predicted by conduction-only models. Furthermore, the melt pool width is increased and the depth is reduced by the action of the Marangoni effect.

However, the effects of Marangoni convection (peak temperature reduction and melt pool geometry change) can be replicated in a heat conduction model by artificially increasing the thermal conductivity in the liquid phase [29]. Karayagiz et al. [30] proposed a heat conduction model for laser -PBF process with the same effects as Marangoni convection by modifying the liquid thermal conductivity with a constant and uniform value or correction factor. They found that the model predicted melt pool dimensions using a correction factor value of 2.5 on the thermal conductivity of liquid Ti-6Al-4V. Hence, the proposed correction was a simple method for including the effects of Marangoni convection without the computational expense of including Marangoni effects into the physics of the model. Using a similar concept, Romano et al. [31] selected a value of correction factor of 15 to modify the value of thermal conductivity of Inconel 718 to replicate the effects of Marangoni convection.

Different values of surface tension gradient are reported in literature. Nikam et al. [32] reported on the correlation between the constant correction factor and surface tension gradient by comparing simulation results from heat conduction and CFD models. A uniform and constant correction factor was used to modify the value of liquid thermal conductivity above the baseline properties for Ti-6Al-4V. The selection criterion for correction factor was based on agreement between peak temperatures. Peak temperature agreement was achieved between models but, correspondingly, there was limited success for agreement between melt pool dimensions: length, width, and depth. Hence, the option of using a constant correction factor was shown to struggle in satisfying all requirements of equality between peak temperatures and melt pool geometries.

It has been shown that Marangoni convection in PBF has similar effects as in welding (that is, increase in melt pool width and reduction in depth) [33]. There is limited evidence of heat conduction models of the PBF process that can satisfy all of the requirements around the geometry of the melt pool. Therefore, the present study aims to bridge this gap by proposing a heat-conduction model with directional correction factors to incorporate the geometry-changing effects of Marangoni convection. In addition, a mesh modification approach is incorporated to give improved predictions of the deposition geometry.

1.2. Aim and Objectives

The aim of the present work is to develop a reduced-physics, heat-conduction model that replicates the melt pool during the deposition process in laser-PBF additive manufacturing. The objectives of the present study include the development of a heat conduction model and an experimental dataset to investigate the applicability of a directional, correction-factor approach to simulate the melt pool geometry. The experimental data (which was developed for a single-layer, multi-track deposition of Ti-6Al-4V) is used to estimate the correction factors. In order to demonstrate the effectiveness of the approach, the proposed method is also tested with PBF data published in literature (single track, single layer), acquired using a different apparatus to the current work and over a wider range of processing parameters.

2. Methodology

The methodology developed in this study involved experimental and simulation approaches. The experimental details of a single-layer multi-track deposition are provided followed by detailed description of the modelling approach.

2.1 Experimental details

2.1.1 Single-layer multi-track deposition

Deposition of single-layer multi-tracks was achieved using a GE Additive Mlab Cusing R machine. The substrate was 91×91×20 mm^3 and was made from wrought, grade 5, Ti6Al4V (microstructure confirmed through etching and optical microscopy, composition confirmed by Optical Emission Spectroscopy). The feedstock powder was plasma-atomised, extra-low interstitial (Grade 23) Ti-6Al-4V powder. The particle size distributions of the powder ranged between 15 to 76 μm, with 85% of the powder ranging in size between 25 to 50 μm. The powder particles, which were highly spherical (circularity > 0.98), provided good flowability. The deposition was carried out in an argon environment maintained with oxygen levels below 0.1%. The process parameters used for this investigation include laser power, P, of 95 W, scanning speed, v, of 900 mm/s, and layer height, L_H, of 25 μm. The hatch spacing was set to 100 μm which allowed a clear gap to be present between neighbouring tracks. Figure 1 shows the plan view of the 5×5 mm^2 single-layer, multi-track deposition coupon. The laser scanning strategy was a bi-directional/zigzag scan [34] over one layer followed by an outline contour scan. Hence, the deposited tracks were initially laid down were parallel to each other but with the laser scanning directions alternating between neighbouring tracks. The contour scan created deposited track around the perimeter of the region of interest. The melt pool created by the

contour scan left a larger melt pool, which is of no specific interest to this study. Through this approach, a total of 39 tracks were available inside the contour scan for measurement of the melt pool dimensions.

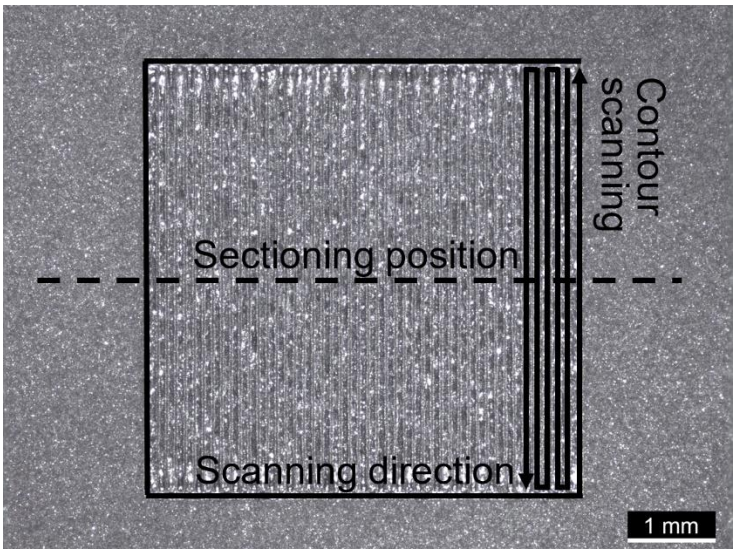

Figure 1 The plan view of the single-layer multi-track deposition.

2.1.2 Sample preparation

After fabrication, the single-layer deposition was sectioned along the centreline of the tracks perpendicular to the scanning direction (cut plane indicated by the broken line in Figure 1). Samples were then hot mounted, ground, and polished with a final stage polishing using 0.06 µm colloidal silica. Finally, the sample was etched with Kroll's reagent to identify the boundaries of the melt pools. The images of the melt pools were captured with an optical microscope in bright field mode and the dimensions of the melt pools were measured.

2.2 Modelling details

The finite element simulation was done using ANSYS Parametric Design Language (APDL) codes specifically developed for the laser-based PBF process.

2.2.1. Governing equations

The governing equation for 3D heat conduction is expressed as:

$$\frac{\partial H}{\partial t} = \nabla [K \nabla T] \qquad (1)$$

Where, H is the enthalpy; t is the time; T is the temperature and K is thermal conductivity.

A modified specific heat method was used to incorporate the effects of latent heat using c_p^* as the modified specific heat parameter for the mushy zone. The details of enthalpy modification are as follows:

$$H(T) = \int_{T_o}^{T} \rho c_p dT \qquad \forall\ T \leq T_S \qquad (2)$$

$$H(T) = \int_{T_o}^{T_S} \rho c_p dT\ + \rho(T_S) c_p^*(T - T_S) \qquad \forall\ T_S < T \leq T_L \qquad (3)$$

$$c_p^* = \left(\frac{c_p(T_S) + c_p(T_L)}{2}\right) + \left(\frac{L}{T_L - T_S}\right) \qquad (4)$$

$$H(T) = \int_{T_o}^{T_S} \rho c_p dT\ + \rho(T_S) c_p^*(T_L - T_S)\ + \int_{T_L}^{T} \rho c_p dT \qquad \forall\ T > T_L \qquad (5)$$

Here, T_0 is ambient temperature; T_S, solidus temperature; T_L, liquidus temperature; L, latent heat of fusion; and ρ, density. At time, $t = 0$ *s*, the initial condition of the substrate material is selected to be at ambient temperature, T_0, of 298.15 K.

A 2D Gaussian heat source model determines the input heat flux, q, applied on the top surface of the powder bed as follows:

$$q = \frac{2AP}{\pi R^2} exp^{\left(\frac{-2r^2}{R^2}\right)}. \qquad (6)$$

Where, P is the laser power; A is absorptivity of the laser beam on the powder bed; R is the radius of the laser spot, and r is the radial distance from the laser beam centre.

To reduce computation time, the region of interest of the substrate was a reduced volume of 6x2x0.6 mm^3. The bottom and side surfaces of the volume were assigned with adiabatic boundary conditions. Convection and radiation boundary conditions were assigned to the top surface over which the powder spreads using the following equations:

$$q_c = h_c(T - T_0) \qquad (7)$$

$$q_r = \varepsilon\sigma(T^4 - T_0^4) \qquad (8)$$

Here, q_c is heat flux due to convection; q_r is heat flux due to radiation; σ is Stefan-Boltzmann constant; ε is the emissivity, and h_c is a convective heat transfer coefficient. Figure 2 shows the main geometry of the volume considered during modelling.

2.2.2. Directional correction factor liquid thermal conductivity

As discussed in the literature review, previous work [30] proposed a uniform correction factor (C_m) to be applied to the thermal conductivity of liquid to mimic the effects of Marangoni convection on the melt pool in a conduction-only model. In order to improve the agreement on melt pool geometry, directional correction factors are proposed for the liquid thermal conductivity in all three Cartesian directions. Therefore, the value of thermal conductivity of

material above liquidus temperature becomes anisotropic due to these artificial changes. Changes to liquid thermal conductivity are implemented as follows:

$$K_{xx}^{*}(T) = C_{mx}K(T) \quad if\ T > T_L \tag{9}$$

$$K_{yy}^{*}(T) = C_{my}K(T) \quad if\ T > T_L \tag{10}$$

$$K_{zz}^{*}(T) = C_{mz}K(T) \quad if\ T > T_L \tag{11}$$

Where, K_{xx}^{*}, K_{yy}^{*}, and K_{zz}^{*} are the modified values of liquid thermal conductivity in X, Y and Z directions, respectively. C_{mx}, C_{my} and C_{mz} are the directional correction factors. In this analysis, X is the direction along the line of travel of the laser, Y is the lateral direction to the laser path parallel to the substrate surface, and Z is the vertical direction, perpendicular to the substrate surface. The final description of liquid thermal conductivity is representative of an anisotropic thermal conductivity and could be described as a 3x3 matrix where the modified thermal conductivities in equations (9) to (11) are diagonal terms. Thermal conductivity values for non-diagonal terms such as K_{xy}, K_{xz}, K_{yx}, K_{yz}, K_{zx}, and K_{zy} are set to zero; hence, the approach is an orthotropic description of anisotropic heat transfer.

2.2.3. Simulation setup

Figure 2 illustrates the 3D geometry and meshing setup used to simulate single-layer multi-track deposition. The geometry of the base having size of 6 mm x 2 mm x 0.6 mm and each powder bed layer having overall geometry of 6 mm x 2 mm x 0.025 mm. Figure 2(b) illustrates the meshing attributes used in the current investigations. The geometry of the base and powder bed layer has been discretised with brick shape, eight-node elements. The mesh sensitivity analysis revealed that mesh height of 25 μm and 10 μm in X and Y directions was suitable. Mesh sizes below this value did not show any significant mesh-dependent changes in the temperature results.

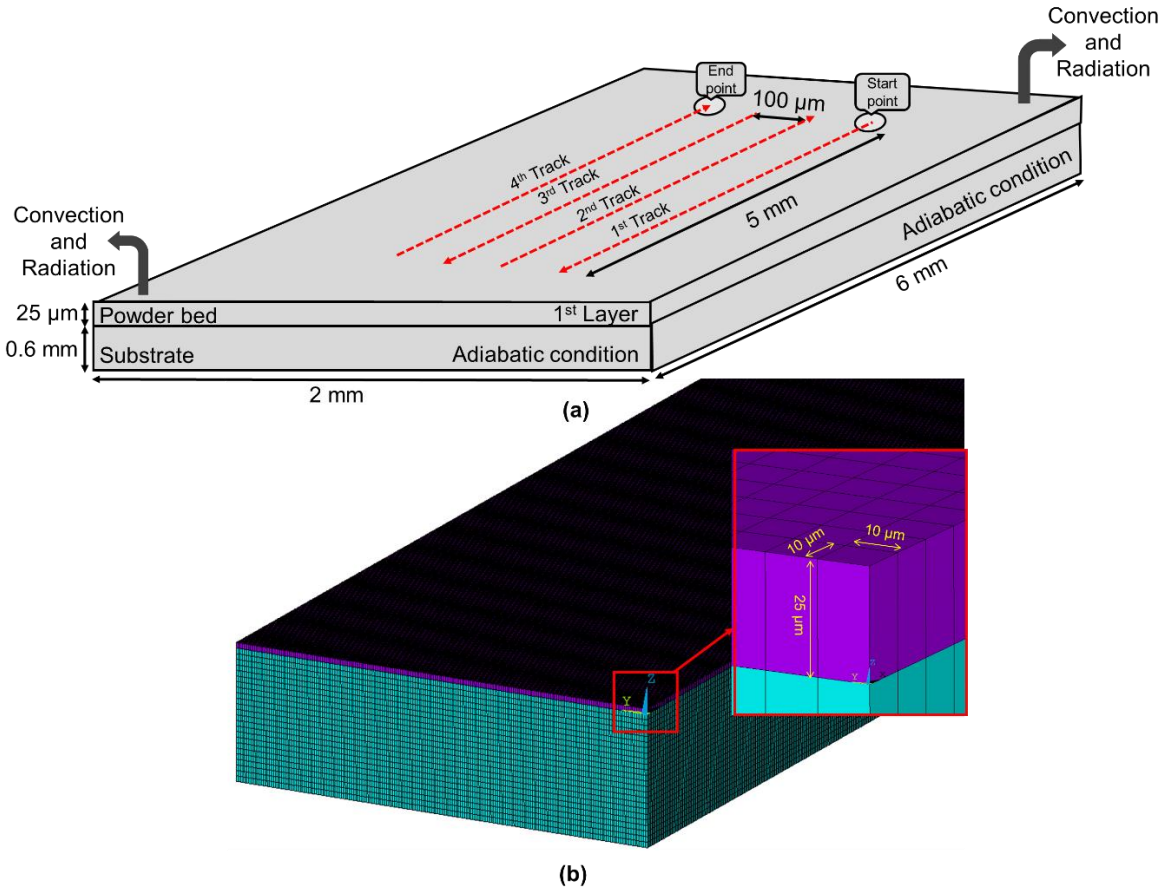

Figure 2 (a) Schematic of 3D geometry used for four single-layer multi-track deposition and (b) details of the meshed geometry.

2.2.4 Modelling the powder before and after solidification

Two configurations of material properties are used to simulate powder as a porous medium (prior to melting) and as bulk (condensed) material in the liquid and solidified states. Figure 3 shows the thermophysical material properties of Ti-6Al-4V used [35]. For property values at temperatures above those reported in the literature, we assumed the property value to be constant at the same value as that given at the highest reported temperature. The powder bed layer is treated as a porous medium; hence, the material properties are modified using the following equations [23]:

$$K_{layer} = K_{bulk}(1-\theta)^n \qquad (12)$$

$$\rho_{layer} = \rho_{bulk}(1-\theta) \qquad (13)$$

Where K_{layer} and ρ_{layer} are the thermal conductivity and density of powder, K_{bulk} and ρ_{bulk} are the baseline thermal properties of the bulk material, θ is the porosity, and n is an empirical

parameter taken from literature taken as being equal to four [36]. Figure 3 shows the adapted powder properties plotted against temperature alongside bulk properties.

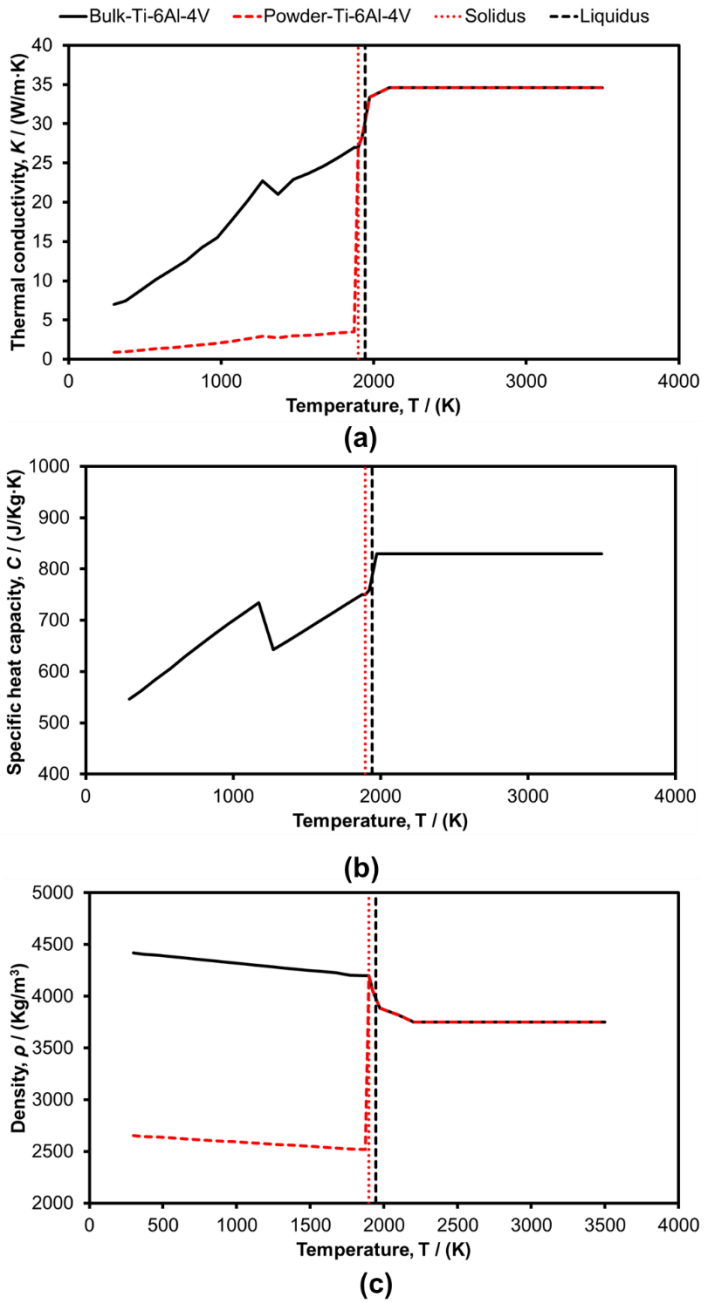

Figure 3 Thermophysical material properties: (a) thermal conductivity, (b) specific heat capacity and (c) density of consolidated Ti-6Al-4V [35] alongside adapted datasets for powder treated as a porous medium.

The transition from porous medium to condensed matter is captured in the simulation with a geometry-driven remeshing process applied to the consolidated layer on the substrate. As demonstrated, the powder layer is modelled using a single-layer of brick-type element with

nodes at the vertices. As heat flux is applied through equation (6) and the powder temperature exceeds the liquidus (i.e., as the powder melts), the positions of the vertices for the elements above the substrate are adjusted to new heights and then considered to be an extension to the substrate's mesh (i.e., the elements are no longer consider to be part of the powder layer). Ellipsoidal geometry is used to calculate the new vertex heights, Z_{new}, of the re-meshed, powder layer brick elements as

$$Z_{new} = N_H \sqrt{1 - \frac{x^2}{a^2} - \frac{y^2}{b^2}} \qquad (14)$$

Where, N_H is the new overall track height; x and y are coordinates of the local reference frame that moves with the point of application of the laser; and a and b are the major and minor axis of the assumed elliptical geometry applied on the x-y plane.

The new overall track height, N_H, is assumed *a priori* in the model setup. In this analysis, empirical evidence is used to set N_H. The major and minor dimensions, a and b, are determined by the physical extents of the simulated melt pool: a is the extent of the melt pool in the x-direction in advance of the local reference frame and b is the extent of the melt pool in the positive y-direction. In the first instance, the computed deposition geometry is symmetrical and, since the melt pool is circular with $a = b$, the geometry approximately resembles sessile drop geometry. As the laser moves in the positive x direction, the final track geometry in the y-z plane (where x=0) is described by the equation $Z = N_H \sqrt{1 - \frac{y^2}{b^2}}$ and this elliptical profile is maintained as the basis of the extruded geometry for the deposited track bead. Thereafter, equation (14) is applied only for the new track bead ahead of the local reference frame, i.e., for $x > 0$. Figure 4 shows the process of track deposition with example of the initial sessile drop and the extruded elliptical geometry that gives the corresponding representation of the track bead.

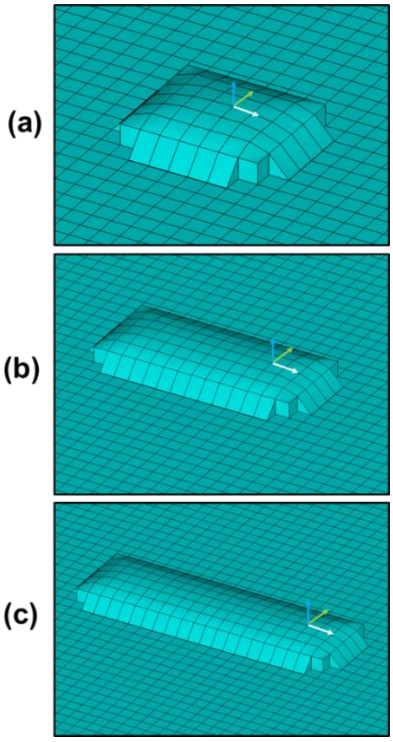

Figure 4 Deposition of track with sessile drop captured at initial time (a) and extruded elliptical geometry at two later times (b) and (c). The axes show the reference position of the laser.

As the powder melts and solidifies, and after the geometry undergoes remeshing, the bulk properties of the material are used as the material is then assumed to be a condensed phase.

2.2.5 Simulation parameters

Thermophysical properties have already been presented in Figure 3. The values of all other process and simulation parameters used are summarized in Table 1.

Table 1. Values of laser-based PBF process parameters and other parameters used in the heat conduction model.

Laser-based PBF process parameters and other parameters	**Symbols**	**Values (Units)**
Laser power	P	95 (W)
Scanning speed	v	900 (mm/s)
Powder bed layer height	L_H	25 (µm)
Layer height after remeshing	N_H	16 (µm)
Laser beam radius	R	0.025 (mm)
Latent heat of fusion	L	365000 (J/Kg) [11]

Solidus temperature	T_s	1873.15 (K)
Liquidus temperature	T_L	1923.15 (K)
Convective heat transfer coefficient	h_c	80 (W/m^2·K)
Emissivity coefficient	ε	0.7
Stefan-Boltzmann constant	σ	5.67 x 10^{-8} (W/m^2·K^4)
Absorption coefficient	A	0.71
Correction factor in *x*-direction	C_{mx}	4
Correction factor in *y*-direction	C_{my}	4
Correction factor in *z*-direction	C_{mz}	17
Initial powder porosity	θ	0.4

Figure 5 depicts the schematic of the melt pool dimensions such as melt pool width (P_w), melt pool length (P_L) and melt pool depth (P_d) for the single-layer single-track deposition. These three dimensions along with the temperature histories are the main outputs from the model.

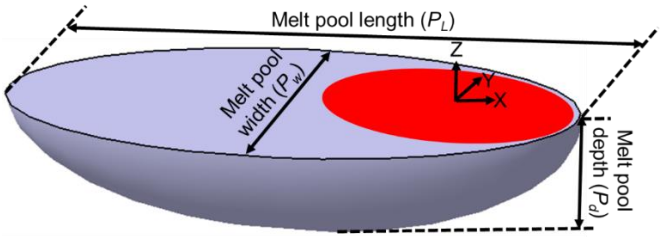

Figure 5 Schematic of melt pool characteristics in single-layer single-track deposition

3. Results

3.1 Experimental melt pool dimensions

Figure 6(a) shows the macro-view of the single-layer multi-track deposition after cross section and etching. The melt pools arising due to contour scan at either end of the deposition are highlighted and are easily recognisable due to their increased depth and high degree of overlap. Other studies have shown that the initial track on a powder bed can have the greatest profile height with subsequent tracks having lower profiles due to powder denudation on the substrate caused by the previously-laid, nearest-neighbour track [37,38]. However, in this study, the tracks within the central region were consistent in their final geometry. Including the two overlapped contour depositions, a total of 49 tracks were deposited. However, only the central 39 tracks were measured to obtain the average width and depth of the melt pools.

Figure 6(b) shows the macrostructure of a typical single-track melt pool used for determining the width and depth of the melt pool. The morphology exhibited by all melt pools is typical for conduction mode [39,40].

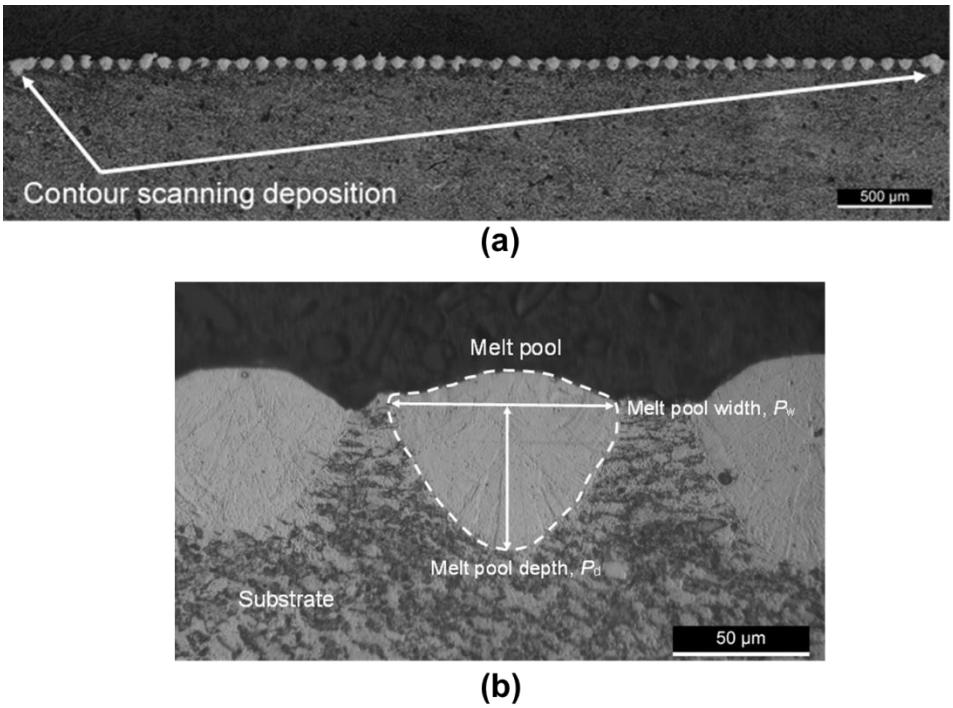

Figure 6 (a) Wide angle cross section view of the single-layer multi-track deposition and (b) detailed view of a typical melt pool with width and depth dimensions annotated.

3.2 Simulated melt pool

Figure 7 depicts the predicted melt pool geometry in grey, where the temperature is above liquidus. The Heat Affected Zone (HAZ) is shown against a thermal colour legend where temperature is below solidus. Four adjacent tracks are simulated as they are laid down in series on the substrate material. After the fourth track the melt pool width and depth reached steady state as no significant changes between third and fourth track were observed. Essentially, each previous track was shown to provide preheat conditions for the next track, but as shown the preheating effect eventually stabilised. The simulated melt pool dimensions were captured at the mid-point of travel for each track (i.e., 2.5 mm). Table 3 shows comparison of simulated and experimentally measured melt pool dimensions. The mean value of melt pool width and depth for the central 39 experimentally deposited tracks as shown in Figure 6(b) were 81 µm and 52 µm, respectively. The stabilised melt pool geometry (track 4) is in good agreement with experimentally measured melt pool dimensions.

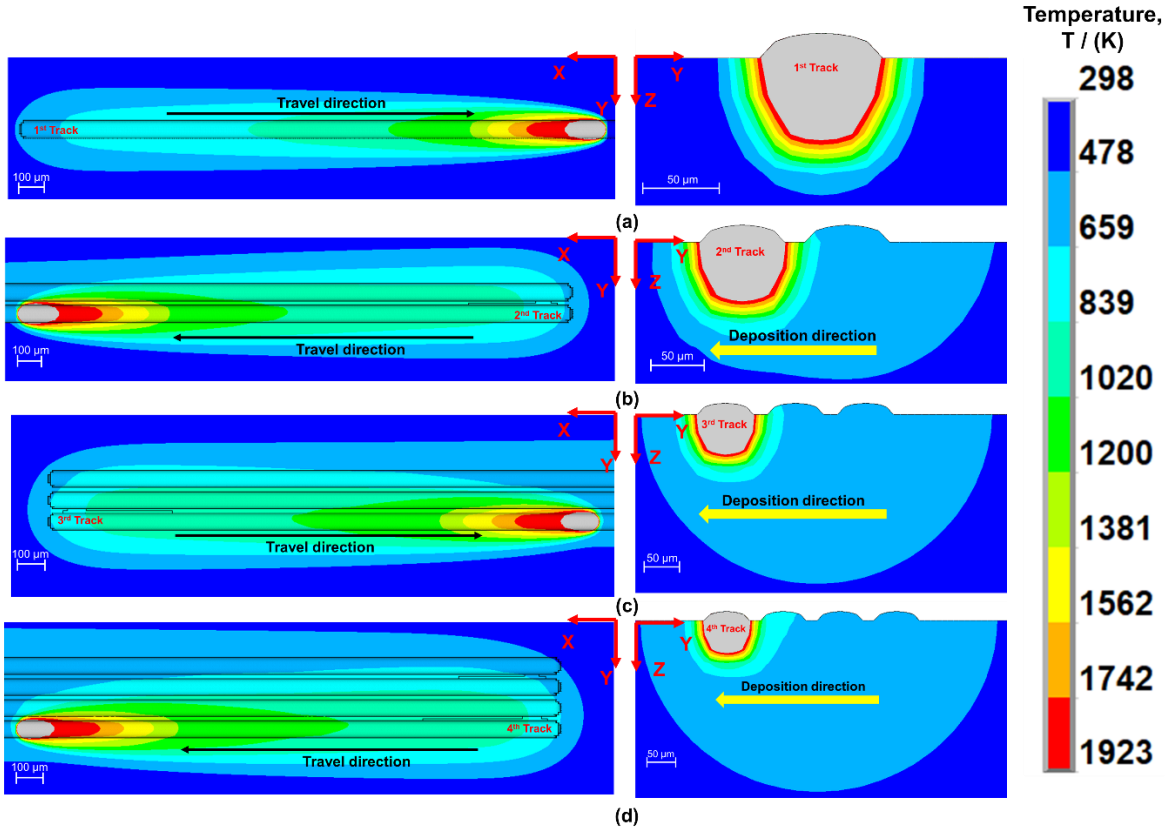

Figure 7 Melt pool geometry (grey coloured region) and HAZ for (a) first, (b) second, (c) third and (d) fourth tracks.

Table 3 Simulated and experimentally measured melt pool dimensions.

Track no.	Simulated melt pool dimensions with directional correction factor		Experimentally measured melt pool dimensions	
	P_w (µm)	P_d (µm)	P_w (µm)	P_d (µm)
1	78.4	53.6	81±4	52±5
2	80.8	56.0		
3	81.2	56.4		
4	81.2	56.8		

3.3 Thermal analysis

Figure 8 gives thermal histories recorded at the start, mid and end point of the first (Fig. 8(a)), second (Fig. 8(b)), third (Fig. 8(c)) and fourth (Fig. 8(d)) tracks. Thermal histories were recorded at the substrate-powder bed interface. It is observed that the temperatures increased along each track as the deposition process continued; however, the peak temperatures trended towards steady state after travelling 1.25 mm from the start point of each track. The thermal history figures also reveal that deposited tracks experienced preheating and reheating from their neighbour during the deposition process.

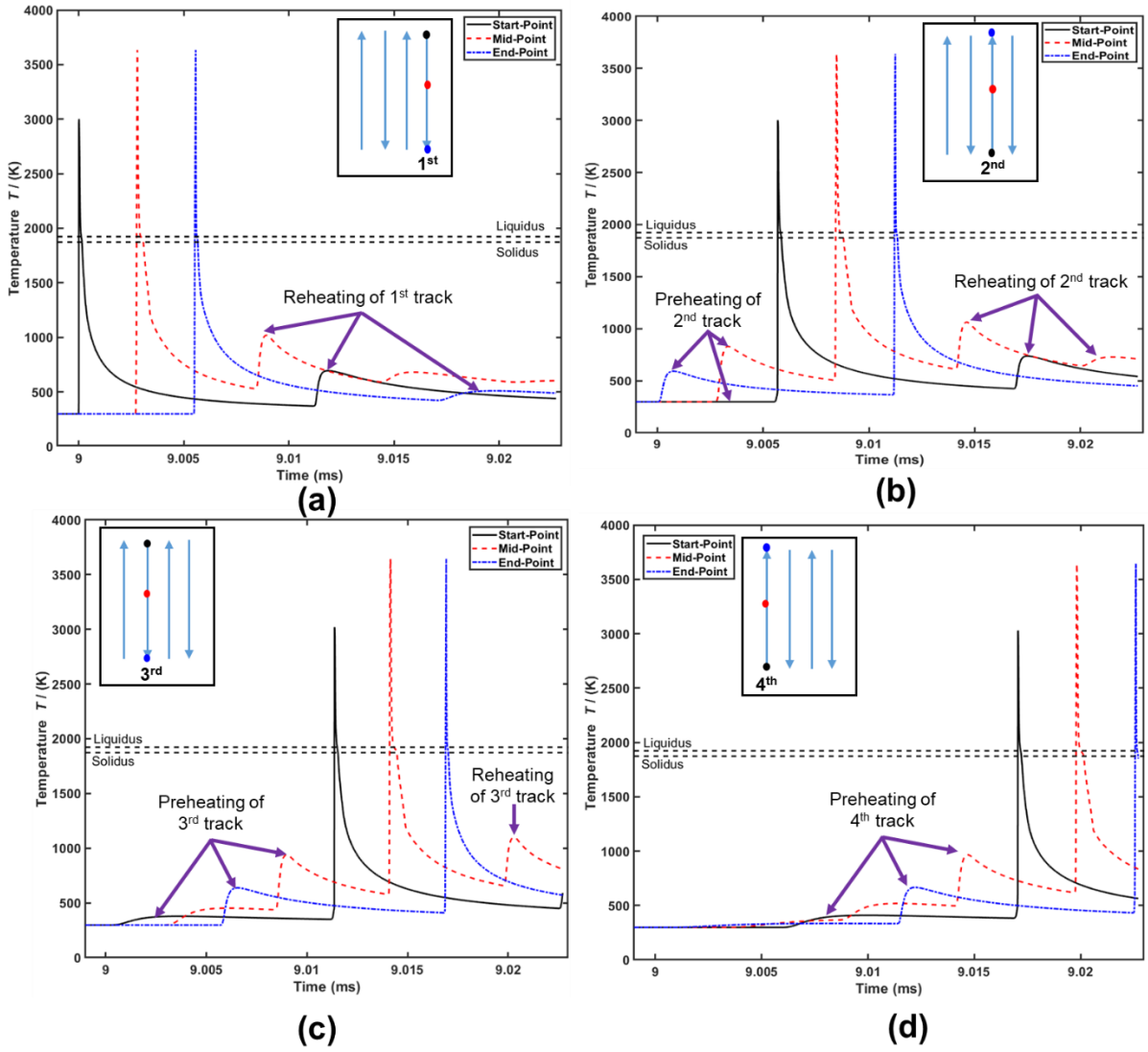

Figure 8 Thermal histories obtained for (a) first, (b) second, (c) third, and (d) fourth track at start, mid and end points.

Figure 9 gives the peak temperatures (Fig. 9(a)) and pre-heating temperatures (Fig. 9(b)) for each track. The peak temperatures (Fig. 9(a)) were recorded at the mid-point of the travel length

i.e., at 2.5 mm along the length of the track. The peak temperatures recorded for first, second, third and fourth track were 3634 K, 3639 K, 3643 K and 3644 K, respectively. As mentioned, it was observed that the peak temperature increased as the adjacent tracks were deposited and reached steady state condition after the third track. After depositing the first track, the pre-heating temperature at the start of the second track was 299 K. The pre-heating temperature at the start point of third and fourth tracks increased to 359 K and 359 K, respectively.

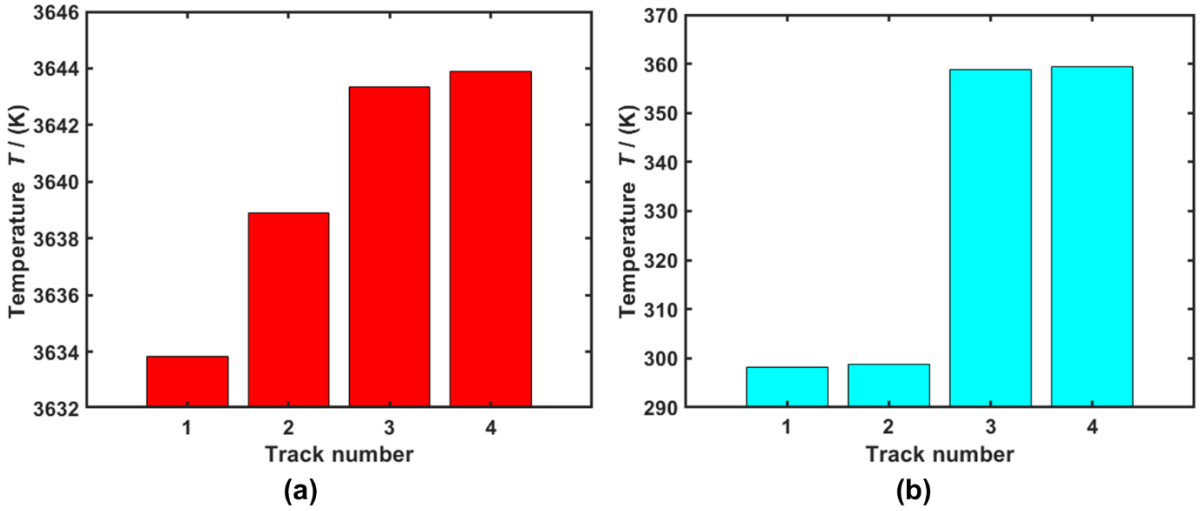

Figure 9 (a) Peak temperatures and (b) preheating preheat temperatures for each track.

3.4 Directional correction factor approach applied to an independent dataset

The approach outlined here, with the directional correction factors selected at C_{mx}= 4, C_{my} = 4, and C_{mz} = 17, gave good agreement with the experimental data sets acquired in our experimental study. However, to test the wider applicability of the approach, it was decided to investigate the approach against an independently acquired dataset from literature. Dilip et al. [41] provide melt pool dimensions for single tracks deposited using an EOS M270 machine with laser spot diameter of 100 μm, layer thickness of 30 μm, and other process parameters as shown. Table 4 shows the corresponding value of directional correction factors used in simulations. Initially, the correction factor values used were the same as determined previously, i.e., C_{mx} = 4, C_{my} = 4 and C_{mz} = 17. But adjustments to the directional correction factors were required to give alternative values of C_{mx} = 21, C_{my} = 21 and C_{mz} = 20. Table 5 provides the comparison of experimental and simulated melt pool geometry along with percentage differences calculated for each case.

Table 4 Process parameters [41] **and directional correction factor values**

No.	Power (W)	Speed (mm/s)	C_{mx}	C_{my}	C_{mz}
1	100	750	4	4	17
2	100	750	21	21	20
3	150	1000			
4	150	750			

Table 5 Comparison of experimental [41] **and simulated melt pool dimensions**

No.	Experimental width (μm)	Experimental depth (μm)	Simulated width (μm)	Simulated depth (μm)	Error in width (μm)	Error in depth (μm)
1	98	32	83.2	44.8	17.7%	28.5%
2	98	32	98.4	31.6	0.4 %	1.3%
3	117	51	121.6	47.6	3.7%	7.1%
4	134	72	136.8	67.9	2%	6%

4. Discussion

The present study investigates a directional correction factor approach applied to a heat conduction model of the laser-PBF process. The method aims to replicate the effects of Marangoni convection on the melt pool geometry, namely, wider and shallower melt pools. Previous studies showed that the desired effects could be qualitatively achieved by artificially and uniformly increasing the thermal conductivity of the liquid phase [30,32]. But it has also been shown that it is difficult to achieve full agreement between all three melt pool major dimensions and peak temperature predictions by comparing to a CFD model with Marangoni convection included [32]. Hence, this work proposes an orthotropic description of anisotropic thermal conductivity in the liquid phase. Practically this was achieved by applying different values of correction factor in X, Y, and Z directions in the melt pool.

Dedicated experimental data for melt pool formation in a single-layer, multi-track experiment was acquired to determine the appropriate values of correction factor. Using the average melt pool width and depth, the values of correction factor in Y (lateral) and Z (normal) direction were found by the trial-and-error. It is reasonable to assume (for practical fitting purposes) that there exists one-to-one correspondence between width and C_{mx}, and depth and C_{mz}.

Because there is no direct experimental data available for the length of the melt pool it was assumed that the correction factor in the X direction, C_{mx}, is the same as that in the Y direction, C_{my}. This assumption permitted the current investigation to proceed, but it should be investigated by suitable means (other than ex-situ metallography) that measures melt pool length.

Correction factors, $C_{mx} = 4$, $C_{my} = 4$ and $C_{mz} = 17$ gave excellent agreement between the model and the experimental data acquired using the MlabR PBF apparatus under the process parameters cited in Table 1. However, this original combination of directional correctional factor gave an error of 17.7% and 28.5% for melt pool width and height, respectively, when compared to the data from Dilip et al. Directional correction factor values were modified to give $C_{mx} = 21$, $C_{my} = 21$ and $C_{mz} = 20$. This new combination of correction factors gave good agreement across a range of processing parameters as shown in Table 5.

This comparison exercise highlights the general applicability of the method, but also shows the importance of selecting unique correction factors on a case-by-case basis. The differences in correction factors for each dataset are likely to be due to differences that existed in the processing conditions for each apparatus. The laser diameter in the dataset acquired on the MlabR apparatus is 50 µm whereas, the laser diameter from the literature dataset is 100 µm. Small differences existed for the layer heights (25 µm on the MlabR and 30 µm on the EoS) and the different powder spreader mechanisms on each machine may have led to further differences in layer height. Hence, the exercise described here of creating and analysing tracks on the substrate during the initial layer is a simple step that is recommended on all builds where calibration of the correction factors is required.

5. Conclusion

The outcomes from this paper were aimed towards the development of a reduced physics, heat conduction model for the laser-PBF process. The focus was to provide a computationally efficient and accurate model for the melt pool. A heat conduction model with an orthotropic description of anisotropic thermal conductivity in the liquid phase can be used to predict melt pool width and depth using calibrated directional correction factors applied along the cartesian directions. The model was initially calibrated against experimental data acquired on an Mlab Cusing R. Simulations gave realistic behaviour in good agreement to experimental data. Transient behaviours such as preheating and reheating were displayed during multi-track deposition.

After comparing with the bespoke experimental dataset comparisons were made with an independent dataset from literature. Recalibration of the directional correction factors was necessary and was shown to be a key step to has to be conducted on a case-by-case basis. Nevertheless, comparing with the data from literature, agreement to within 7% (approx.) was achieved across four combinations of parameter sets: power levels at 100 and 150 W, and scanning speeds at 750 and 1000 mm/s.

This approach will be useful for those who wish for a quick, yet accurate prediction of the melt pool width and depth. When appropriately calibrated, this model will be useful in providing an improved determination of the process parameter operating windows to avoid lack of fusion defects. For example, the model could be used to give improvements beyond the simple analytical expressions for melt pool geometry used in literature [3].

Acknowledgments

This research (SN, HW, RH, JQ, SMF) has been supported by the INTERREGVA (Project ID: IVA5055, Project Reference Number: 047). The North West Centre for Advanced Manufacturing (NW CAM) project is supported by the European Union's INTERREG VA Programme, managed by the Special EU Programmes Body (SEUPB). The views and opinions in this document do not necessarily reflect those of the European Commission or the Special EU Programmes Body (SEUPB).

References

[1] M. Tang, P.C. Pistorius, J.L. Beuth, Prediction of lack-of-fusion porosity for powder bed fusion, Addit. Manuf. 14 (2017) 39–48. https://doi.org/10.1016/j.addma.2016.12.001.

[2] M. Tang, P.C. Pistorius, C. Montgomery, J. Beuth, Build Rate Optimization for Powder Bed Fusion, J. Mater. Eng. Perform. 28 (2019) 641–647. https://doi.org/10.1007/s11665-018-3647-5.

[3] J. V. Gordon, S.P. Narra, R.W. Cunningham, H. Liu, H. Chen, R.M. Suter, J.L. Beuth, A.D. Rollett, Defect structure process maps for laser powder bed fusion additive manufacturing, Addit. Manuf. 36 (2020) 101552. https://doi.org/10.1016/j.addma.2020.101552.

[4] D. Rosenthal, Mathematical theory of heat distribution during welding and cutting, Weld. J. 20 (1941) 220–234.

[5] J. Goldak, A. Chakravarti, M. Bibby, A new finite element model for welding heat sources, Metall. Trans. B. 15 (1984) 299–305. https://doi.org/10.1007/BF02667333.

[6] Y. Shu, D. Galles, O.A. Tertuliano, B.A. McWilliams, N. Yang, W. Cai, A.J. Lew, A critical look at the prediction of the temperature field around a laser-induced melt pool on metallic substrates, Sci. Rep. 11 (2021) 1–11. https://doi.org/10.1038/s41598-021-91039-z.

[7] R. Wang, Y. Lei, Y. Shi, Keyhole modeling during laser deep penetration welding, Appl. Mech. Mater. 29–32 (2010) 252–257. https://doi.org/10.4028/www.scientific.net/AMM.29-32.252.

[8] J. Jakumeit, G. Zheng, R. Laqua, S.J. Clark, J. Zielinski, J.H. Schleifenbaum, P.D. Lee, Modelling the complex evaporated gas flow and its impact on particle spattering during laser powder bed fusion, Addit. Manuf. 47 (2021) 102332. https://doi.org/10.1016/j.addma.2021.102332.

[9] C.L.A. Leung, S. Marussi, R.C. Atwood, M. Towrie, P.J. Withers, P.D. Lee, In situ X-ray imaging of defect and molten pool dynamics in laser additive manufacturing, Nat. Commun. 9 (2018) 1–9. https://doi.org/10.1038/s41467-018-03734-7.

[10] C. Panwisawas, C. Qiu, M.J. Anderson, Y. Sovani, R.P. Turner, M.M. Attallah, J.W. Brooks, H.C. Basoalto, Mesoscale modelling of selective laser melting: Thermal fluid dynamics and microstructural evolution, Comput. Mater. Sci. 126 (2017) 479–490. https://doi.org/10.1016/j.commatsci.2016.10.011.

[11] W. Huang, Y. Zhang, Finite element simulation of thermal behavior in single-track multiple-layers thin wall without-support during selective laser melting, J. Manuf. Process. 42 (2019) 139–148. https://doi.org/10.1016/j.jmapro.2019.04.019.

[12] C.C. Tseng, C.J. Li, Numerical investigation of interfacial dynamics for the melt pool of Ti-6Al-4V powders under a selective laser, Int. J. Heat Mass Transf. 134 (2019) 906–919. https://doi.org/10.1016/j.ijheatmasstransfer.2019.01.030.

[13] S. Shrestha, Y. Kevin Chou, A Numerical Study on the Keyhole Formation During Laser Powder Bed Fusion Process, J. Manuf. Sci. Eng. 141 (2019) 1–9. https://doi.org/10.1115/1.4044100.

[14] C.H. Fu, Y.B. Guo, Three-Dimensional Temperature Gradient Mechanism in Selective Laser Melting of Ti-6Al-4V, J. Manuf. Sci. Eng. Trans. ASME. 136 (2014) 1–7. https://doi.org/10.1115/1.4028539.

[15] M.J. Ansari, D.S. Nguyen, H.S. Park, Investigation of SLM process in terms of temperature distribution and melting pool size: Modeling and experimental approaches, Materials (Basel). 12 (2019) 1–18. https://doi.org/10.3390/ma12081272.

[16] B. Xiao, Y. Zhang, Marangoni and Buoyancy effects on direct metal laser sintering with a moving laser beam, Numer. Heat Transf. Part A Appl. 51 (2007) 715–733. https://doi.org/10.1080/10407780600968593.

[17] M. Xia, D. Gu, G. Yu, D. Dai, H. Chen, Q. Shi, Porosity evolution and its thermodynamic mechanism of randomly packed powder-bed during selective laser melting of Inconel 718 alloy, Int. J. Mach. Tools Manuf. 116 (2017) 96–106. https://doi.org/10.1016/j.ijmachtools.2017.01.005.

[18] T. Heeling, M. Cloots, K. Wegener, Melt pool simulation for the evaluation of process parameters in selective laser melting, Addit. Manuf. 14 (2017) 116–125. https://doi.org/10.1016/j.addma.2017.02.003.

[19] T.N. Le, Y.L. Lo, Z.H. Lin, Numerical simulation and experimental validation of melting and solidification process in selective laser melting of IN718 alloy, Addit. Manuf. 36 (2020) 101519. https://doi.org/10.1016/j.addma.2020.101519.

[20] S.A. Khairallah, A.T. Anderson, A. Rubenchik, W.E. King, Laser powder-bed fusion additive manufacturing: Physics of complex melt flow and formation mechanisms of pores, spatter, and denudation zones, Acta Mater. 108 (2016) 36–45. https://doi.org/10.1016/j.actamat.2016.02.014.

[21] Y. Li, D. Gu, Thermal behavior during selective laser melting of commercially pure titanium powder: Numerical simulation and experimental study, Addit. Manuf. 1–4 (2014) 99–109. https://doi.org/10.1016/j.addma.2014.09.001.

[22] A. Foroozmehr, M. Badrossamay, E. Foroozmehr, S. Golabi, Finite Element Simulation of Selective Laser Melting process considering Optical Penetration Depth of laser in powder bed, Mater. Des. 89 (2016) 255–263. https://doi.org/10.1016/j.matdes.2015.10.002.

[23] L.E. Loh, C.K. Chua, W.Y. Yeong, J. Song, M. Mapar, S.L. Sing, Z.H. Liu, D.Q. Zhang, Numerical investigation and an effective modelling on the Selective Laser Melting (SLM) process with aluminium alloy 6061, Int. J. Heat Mass Transf. 80 (2015) 288–300. https://doi.org/10.1016/j.ijheatmasstransfer.2014.09.014.

[24] Y. Huang, L.J. Yang, X.Z. Du, Y.P. Yang, Finite element analysis of thermal behavior of metal powder during selective laser melting, Int. J. Therm. Sci. 104 (2016) 146–157. https://doi.org/10.1016/j.ijthermalsci.2016.01.007.

[25] C. Teng, H. Gong, A. Szabo, J.J.S. Dilip, K. Ashby, S. Zhang, N. Patil, D. Pal, B. Stucker, Simulating melt pool shape and lack of fusion porosity for selective laser melting of cobalt

chromium components, J. Manuf. Sci. Eng. Trans. ASME. 139 (2017). https://doi.org/10.1115/1.4034137.

[26] N.E. Hodge, R.M. Ferencz, R.M. Vignes, Experimental comparison of residual stresses for a thermomechanical model for the simulation of selective laser melting, Addit. Manuf. 12 (2016) 159–168. https://doi.org/10.1016/j.addma.2016.05.011.

[27] M. Liu, L.N.S. Chiu, C. Vundru, Y. Liu, A. Huang, C. Davies, X. Wu, W. Yan, A characteristic time-based heat input model for selective laser melting, Addit. Manuf. 44 (2021) 102026. https://doi.org/10.1016/j.addma.2021.102026.

[28] L. Aucott, H. Dong, W. Mirihanage, R. Atwood, A. Kidess, S. Gao, S. Wen, J. Marsden, S. Feng, M. Tong, T. Connolley, M. Drakopoulos, C.R. Kleijn, I.M. Richardson, D.J. Browne, R.H. Mathiesen, H. V. Atkinson, Revealing internal flow behaviour in arc welding and additive manufacturing of metals, Nat. Commun. 9 (2018) 1–7. https://doi.org/10.1038/s41467-018-07900-9.

[29] C. Lampa, A.F.H. Kaplan, J. Powell, C. Magnusson, An analytical thermodynamic model of laser welding, J. Phys. D. Appl. Phys. 30 (1997) 1293–1299. https://doi.org/10.1088/0022-3727/30/9/004.

[30] K. Karayagiz, A. Elwany, G. Tapia, B. Franco, L. Johnson, J. Ma, I. Karaman, R. Arróyave, Numerical and experimental analysis of heat distribution in the laser powder bed fusion of Ti-6Al-4V, IISE Trans. 51 (2019) 136–152. https://doi.org/10.1080/24725854.2018.1461964.

[31] J. Romano, L. Ladani, M. Sadowski, Laser Additive Melting and Solidification of Inconel 718: Finite Element Simulation and Experiment, JOM. 68 (2016) 967–977. https://doi.org/10.1007/s11837-015-1765-1.

[32] S.H. Nikam, J. Quinn, S. McFadden, A simplified thermal approximation method to include the effects of Marangoni convection in the melt pools of processes that involve moving point heat sources, Numer. Heat Transf. Part A Appl. 79 (2021) 537–552. https://doi.org/10.1080/10407782.2021.1872257.

[33] M. Jamshidinia, F. Kong, R. Kovacevic, Numerical modeling of heat distribution in the electron beam melting® of Ti-6Al-4V, J. Manuf. Sci. Eng. Trans. ASME. 135 (2013) 1–14. https://doi.org/10.1115/1.4025746.

[34] H. Jia, H. Sun, H. Wang, Y. Wu, H. Wang, Scanning strategy in selective laser melting (SLM): a review, Int. J. Adv. Manuf. Technol. 113 (2021) 2413–2435. https://doi.org/10.1007/s00170-021-06810-3.

[35] K.C. Mills, Recommended Values of Thermophysical Properties for Selected Commercial Alloys, Woodhead Publishing Limited, Abington, Cambridge, England, 2002. https://doi.org/10.1533/9781845690144.205.

[36] J. Yin, H. Zhu, L. Ke, W. Lei, C. Dai, D. Zuo, Simulation of temperature distribution in single metallic powder layer for laser micro-sintering, Comput. Mater. Sci. 53 (2012) 333–339. https://doi.org/10.1016/j.commatsci.2011.09.012.

[37] I. Yadroitsev, P. Bertrand, G. Antonenkova, S. Grigoriev, I. Smurov, Use of track/layer morphology to develop functional parts by selective laser melting, J. Laser Appl. 25 (2013) 052003. https://doi.org/10.2351/1.4811838.

[38] M.J. Matthews, G. Guss, S.A. Khairallah, A.M. Rubenchik, P.J. Depond, W.E. King, Denudation of metal powder layers in laser powder bed fusion processes, Acta Mater. 114 (2016) 33–42. https://doi.org/10.1016/j.actamat.2016.05.017.

[39] J. Yang, J. Han, H. Yu, J. Yin, M. Gao, Z. Wang, X. Zeng, Role of molten pool mode on formability, microstructure and mechanical properties of selective laser melted Ti-6Al-4V alloy, Mater. Des. 110 (2016) 558–570. https://doi.org/10.1016/j.matdes.2016.08.036.

[40] E. Soylemez, High deposition rate approach of selective laser melting through defocused single bead experiments and thermal finite element analysis for Ti-6Al-4V, Addit. Manuf. 31 (2020) 100984. https://doi.org/10.1016/j.addma.2019.100984.

[41] J.J.S. Dilip, S. Zhang, C. Teng, K. Zeng, C. Robinson, D. Pal, B. Stucker, Influence of processing parameters on the evolution of melt pool, porosity, and microstructures in Ti-6Al-4V alloy parts fabricated by selective laser melting, Prog. Addit. Manuf. 2 (2017) 157–167. https://doi.org/10.1007/s40964-017-0030-2.